



# High temperature mechanical integrity of selective laser melted alloy 718 evaluated by slow strain rate tests

Dunyong Deng, Ru Lin Peng, Johan Moverare<sup>\*</sup>

*Division of Engineering Materials, Department of Management and Engineering, Linköping University, SE, 58183, Linköping, Sweden*

## ARTICLE INFO

### Keywords:

IN718  
Selective laser melting (SLM)  
Creep  
Environment-assisted grain boundary embrittlement  
Slow strain rate test  
Cavitation  
Surface energy

## ABSTRACT

Strain rate dependent deformation behaviours of selective laser melted Alloy 718 (IN718) are systematically studied at 550 and 650 °C by slow strain rate testing, with a forged counterpart as a reference. Selective laser melted IN718 shows significant susceptibility to intergranular cavitation, resulting in ductility degradation with decreasing strain rate. Detailed fractography and cross section inspections are employed to identify the damage mechanisms. Creep rates are also estimated and compared with the conventional counterparts. The possible critical factors for the inferiority of time dependent damage resistance of selective laser melted IN718 are discussed.

## 1. Introduction

During the past years, manufacturing nickel-base (Ni-base) superalloys components via additive manufacturing (AM) for high temperature applications has attracted significant interests in the aero and energy industries. Weldability of Ni-base superalloy is a prominent concern in the AM fields. Among the Ni-base superalloys used in AM processes, especially in the selective laser melting (SLM) process, Alloy 718 (IN718) is considerable successful due to its outstanding weldability. IN718 is in principle strengthened by  $\gamma''$ , which has relatively sluggish precipitation kinetics and therefore imparts the weldability. With the years of development, one can see in the literature that the focus of SLM IN718 research changes from the microstructure and monotonic mechanical property studies (Jia and Gu, 2014; Lu et al., 2015; Zhang et al., 2015; Chlebus et al., 2015; Trosch et al., 2016; Deng et al., 2018) to fatigue (Balachandramurthi et al., 2018, 2019; Witkin et al., 2019a; Pei et al., 2019) and creep (McLouth et al., 2020; Popovich et al., 2018; Xu et al., 2018; Kuo et al., 2018a; Shi et al., 2019; Witkin et al., 2019b) studies.

Interestingly, with comparison in the cited literature above, one can find that the monotonic tensile properties of SLM IN718 are comparable to the wrought counterparts, while time-dependent properties (Kuo et al., 2018b; Witkin et al., 2019b), especially minimum creep rate and ductility at elevated temperature, are rather inferior to wrought counterparts. This indicates that the mechanical properties of SLM IN718 are very sensitive to the time-dependent damage at elevated temperature. However, it is still not clear how the degradation mechanism evolves from the short-term monotonic tensile test to the long-term sustained load test.

In addition, all the aforementioned creep tests are conducted at 650 °C, which is a typical and reasonable temperature for thermal activation process of creep damage. However, the previous work by the authors (Deng et al., 2019) has shown that for SLM IN718 creep damage is even activated at 550 °C in a time-dependent cracking test, while it is environmental (dynamic) embrittlement damage for a forged counterpart at the same test condition. Such a susceptibility of Alloy 718 to dynamic embrittlement has been widely reported in

<sup>\*</sup> Corresponding author.

E-mail address: [johan.moverare@liu.se](mailto:johan.moverare@liu.se) (J. Moverare).

(Krupp et al., 2003, 2004, 2017; Schlesinger et al., 2017). The embrittlement is due to the reduced grain boundary cohesion by stress-assisted diffusion of oxygen and surface-adsorption at grain boundaries. The dynamic embrittlement resistance can be improved by increasing the Coincidence Site Lattice (CSL) boundaries fractions in the materials (Krupp, 2008; Krupp et al., 2005). However, the fractions of the CSL boundaries and random high angle grain boundaries alone in the SLM 718 might accelerate the crack propagation under the dynamic embrittlement mechanism, but should not change the susceptibility to creep damage at 550 °C. Creep strain rate can dramatically increase with reducing the test sample sizes to nanoscale, by introducing a larger ratio of free surface area to bulk volume. The enhanced nanoscale creep is dominated by surface diffusion, since free surface has 200 higher times of diffusion coefficient than grain boundary (Choi et al., 2013; Yoo et al., 2012). However, such a possibility is not applicable to the activation of creep at 550 °C for SLM IN718, given that the test sample size is at millimetre scale in Deng et al. (2019). The other possibility associated with precipitate-coarsening discussed in Morra et al. (2009); Basirat et al. (2012) does not explain the situation well, since no microstructure changes are observed during the time-dependent cracking test of SLM IN718. The exact mechanism for activating creep damage at a low temperature is not well-understood so far, but it seems to be consistent with the aforementioned inferior creep resistance of SLM IN718.

Therefore, the present research is motivated to study how the mechanical properties change with strain rates, and then aims to gain better understanding of the time-dependent deformation behaviour of SLM IN718 at elevated temperatures. Specifically, tensile tests will be performed at the strain rates of  $10^{-3}$ ,  $10^{-4}$ ,  $10^{-5}$  and  $10^{-6}$ /s at 550 °C and 650 °C. With reducing the strain rate, more interactions of microstructure, environment and load are expected, and the susceptibility to environmental or creep damage can be shown. Such a slow strain rate test (SSRT) technique has been widely used to test stress corrosion cracking susceptibility of materials in corrosive environment (Henthorne, 2016). Also, in the Xu et al. (2019) it has been shown that with SSRT technique, the creep performance can be evaluated within a relatively short experimental time for a high strength AM Ni-base superalloy; substantially higher strain rate sensitivity in Li et al. (2019) and different deformation behaviours in Li et al. (2020); Lindström et al. (2020); Ghorbanpour et al. (2020) have been shown in AM alloys, comparing to the conventional counterparts. Consequently, the present study will be able to 1) map the mechanical properties of SLM IN718 with regards to strain rates and temperatures, and 2) identify the time-dependent damage mechanism active and responsible for inferior creep properties with comparison of a forged counterpart.

## 2. Experimental

### 2.1. Material and heat treatment

Gas atomized IN718 powder with the nominal size less than 65 µm was used as the raw material for the SLM process. The nominal chemical composition of the gas atomized IN718 powder is given in Table 1. The manufacturing of the samples was performed in an argon atmosphere in an EOS M290 machine, with the recommended standard parameter from EOS. As shown in Fig. 1a, rectangular bars were built horizontally and vertically for the anisotropic properties study. These rectangular bars were removed directly from the build plate when the building process was finished, and were then subjected to heat treatment before being sent for machining into tensile test bars (see Fig. 1b). The tensile test bars made from the horizontally-built and vertically-built blocks will hereafter be named as HB and VB specimens, respectively. The heat treatment was selected based on our previous microstructure study (Deng et al., 2018) giving a similar monotonic strength to the commercial forged counterpart. The heat treatment routine included 1) homogenization step at 1080 °C for 1h, 2) solution step at 980 °C for 1h and 3) standard double ageing step at 720 °C for 8h + 50 °C/h furnace cool to 620 °C + 620 °C for 8h. The forged counterpart was heat treated as per AMS 5663 standard, including a solution step at 945 °C for 1h and a standard double ageing step.

### 2.2. Slow strain rate test

Slow strain rate tensile tests were performed as per standard practice ASTM G129-00 on an Instron 5982 machine with maximum 100 kN capacity in lab air. Strain rate was actually set by constant displacement rate of loading unit, and for example, the strain rate of  $10^{-3}$ /s corresponds to the displacement rate of 0.025 mm/s. Strain was measured with Instron 7361C extensometer before strain reached 5%, after which the strain data was read from the displacement. The heating system attached to the tension rig is an Instron SF-16 resistance wire wound furnace with 3 heating zones, and also a Type-K thermocouple was attached to the centre of the specimen to ensure the accurate thermal condition as set. Before starting the tests, the temperature was stabilized for 2 h for the homogeneous thermal distribution through the whole specimens.

Note that, even though only one test was performed for each test condition, the slow strain rate test result present in the following is reliable and representative of the material's intrinsic behaviours. Both metallurgical exceptions and previous tensile test result (Deng

**Table 1**  
Nominal chemical composition of the gas atomized IN718 powder.

Element	Ni	Cr	Fe	Nb	Mo	Co	Ti	Al
wt.%	50 ~55	17.0 ~21.0	Bal.	4.75 ~5.5	2.8 ~3.3	<1.0	0.65 ~1.15	0.20 ~0.80
Element	Mn	Si	Cu	C	P	S	B	
wt.%	<0.35	<0.35	<0.3	<0.08	<0.015	<0.0015	<0.006	

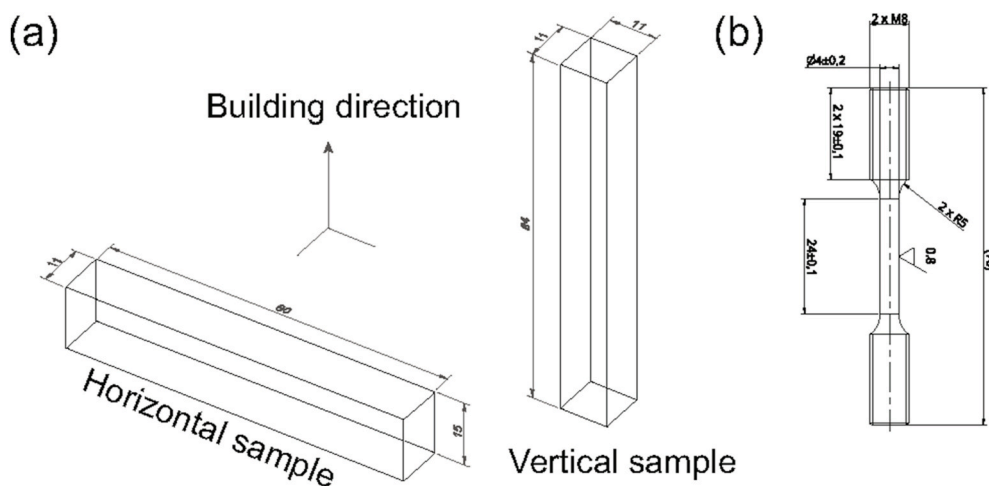


**Fig. 1.** (a) Geometries of the as-built horizontally and vertically built rectangular bars, and the building direction (BD) is also indicated. (b) Geometry of tensile test bar. Then tensile test bars made from the Horizontal-Built and Vertically-Built blocks will be named as HB and VB specimens, respectively.

et al., 2018) indicate the ignorable amount of process-related defects and good mechanical properties statistics. Similarly, the surprising ductility degradation shown in the following has also been reported in Kuo et al. (2017), suggesting that the extremely poor time-dependent ductility degradation is the material's intrinsic behaviour, but not due to scattering of test data.

### 2.3. Fractography and metallography

Fractography was performed using Leica M205C stereo optical microscope (OM) along with Hitachi SU70 FEG scanning electron microscope (SEM). Also the fracture test bars were cut into two halves along the loading direction for metallographic studies of the cross sections. The cross sections were mounted and then polished. The microstructures were characterized with the Hitachi SU70 SEM in both secondary/backscatter modes.

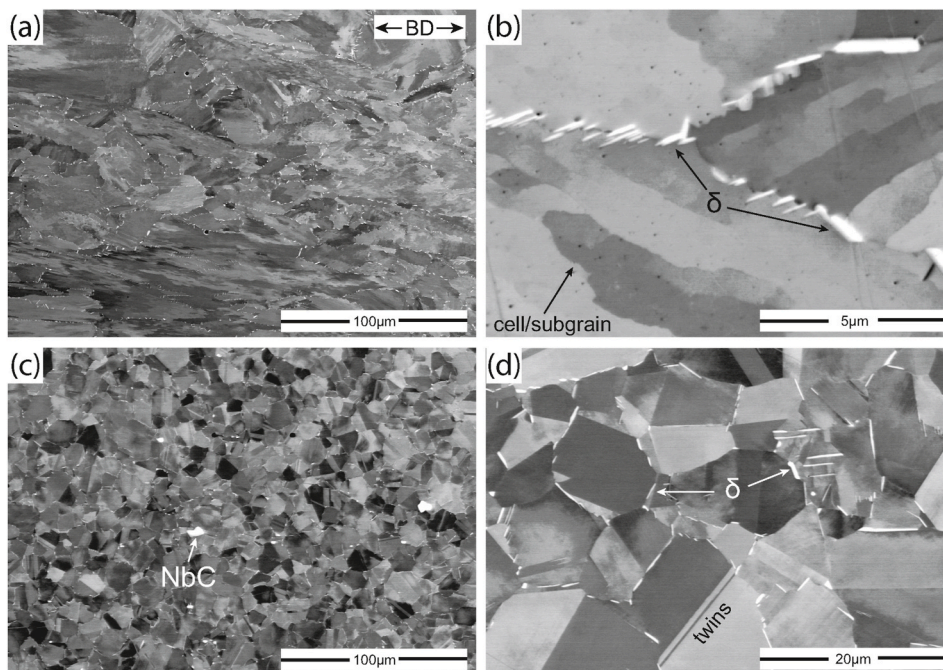


**Fig. 2.** (a) and (c) showing the microstructures of SLM and forged specimens before SSRT tests. (b) and (d) are the enlarged views from (a) and (c) respectively, showing the grain boundary  $\delta$  precipitates, cell/subgrain and twins.

### 3. Results

#### 3.1. Microstructures before SSRT tests

The microstructures of SLM and forged specimens are shown in Fig. 2 a and c, respectively. Generally, the forged counterpart is equiaxed with the average grain size of  $9\ \mu\text{m}$  and with a significant amount of twins. Most grain boundaries are decorated with needle-like  $\delta$  precipitates, as shown in Fig. 2d. Differently, even though a homogenization step of  $1080\ ^\circ\text{C}$  for 1 h is included in the heat-treatment routine for the SLM material, recovery or grain growth is barely found in the as heat-treated SLM microstructure (see Fig. 2a), and the cell/subgrain structure completely remains. Generally, the SLM grains are neither completely equiaxed nor perfectly columnar, instead they are irregular and mostly have the grain boundaries elongated along the building direction. And for the detailed comparison on the spatial distribution of elongated grains between SLM HB and VB specimens, please refer to (Deng et al., 2018). As shown in Fig. 2b, needle-like  $\delta$  phases are present in most of the grain boundaries, and the size is comparatively smaller than that of the forged counterpart. For the dislocation configurations in the SLM and forged materials, please refer to (Deng et al., 2020). The dislocation configuration differences are not discussed in details since that cannot contribute to the noticeable mechanical responses in the SSRT test.

#### 3.2. SSRT results

The tensile stress-strain curves for SLM HB, SLM VB and forged specimens tested at  $550\ ^\circ\text{C}$  are shown in Fig. 3 a, b and c respectively. The tensile properties data are summarized in Table 2. The strain rate effect on the time-dependent tensile properties is generally ignorable when decreasing the strain rate from  $10^{-3}/\text{s}$  to  $10^{-4}/\text{s}$  for both SLM HB and forged specimens, since the strain to fracture does not significantly change between these two strain rate conditions. With this regard, the quasi-static tensile properties for SLM HB, SLM VB and forged counterparts are comparable. However, with further decreasing the strain rate to  $10^{-5}/\text{s}$  and  $10^{-6}/\text{s}$ , reduction in ductilities of SLM HB and SLM VB specimens are significant. Differently, the strain rate effect in ductility reduction for forged specimen is only noticeable at  $10^{-6}/\text{s}$ . On the other hand, it seems that strain rate affects only ductility at the temperature of  $550\ ^\circ\text{C}$ , while yield strength and ultimate strength are not affected.

At  $650\ ^\circ\text{C}$  the strain rate effects become more significant than at  $550\ ^\circ\text{C}$ . Both ductility and strength decrease considerably with strain rate for SLM specimens (see Table 3). Note that, as shown in Fig. 4a, the SLM HB specimens fracture immediately at the yielding points at the strain rates of  $10^{-5}/\text{s}$  and  $10^{-6}/\text{s}$ , showing extremely poor ductility. SLM VB specimen is still able to maintain plasticity to some degree at the strain rate of  $10^{-6}/\text{s}$ , even though ductility is also significantly reduced. Differently, the forged counterpart shows a ductility recover when strain rate decreasing from  $10^{-5}/\text{s}$  to  $10^{-6}/\text{s}$ .

#### 3.3. Fractography and environment-assisted fracture

At elevated temperature, environment-assisted fracture in Ni-base alloy is usually in the form of brittle intergranular cracking, and is usually in dark-blue colour on grain surfaces due to the presence of thin oxides film. All the fracture surfaces after tests at  $550\ ^\circ\text{C}$  are shown in Fig. 5. Dimple but no dark-blue environment-assisted degradation is found on all fracture surfaces at the strain rates of  $10^{-3}/\text{s}$  and  $10^{-4}/\text{s}$ . The brittle environmental fracture is only present in the  $10^{-5}/\text{s}$  and  $10^{-6}/\text{s}$  cases, as dash-outlined in Fig. 5. At  $10^{-6}/\text{s}$ , one can see that the dark-blue areas are larger than at  $10^{-5}/\text{s}$  strain rate, due to the longer time to fracture. And for comparison (see Table 2), the SLM specimens develop less environment-assisted fracture areas than the forged specimens at  $550\ ^\circ\text{C}$ .

At  $650\ ^\circ\text{C}$ , all the fracture surfaces of SLM specimens are completely in dark-blue colour, as seen in Fig. 6. In these cases, it is not possible to distinguish the environmental degradation region simply by colour as in the  $550\ ^\circ\text{C}$  cases. It is believed that the SLM materials mostly fail in the intergranular manner, as combined with the cross section inspection in the following. Both dimpled intergranular fracture (see Fig. 7a) and smooth intergranular fracture (see Fig. 7b) can be found. It is suggested that the dimple feature gradually fades with increasing loading time to fracture. Differently, on the forged fracture surfaces, the progressive development of environment-assisted intergranular fracture is obvious with strain rates from  $10^{-3}/\text{s}$  to  $10^{-5}/\text{s}$ , accompanying the reduction of

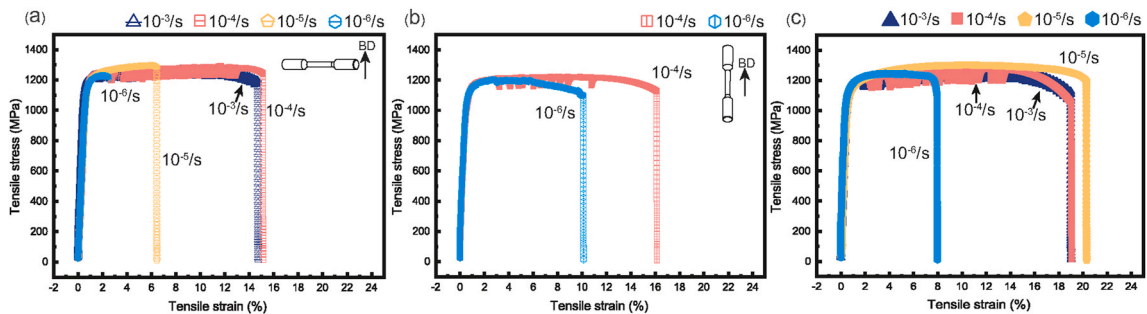


**Fig. 3.** Tensile stress-strain curves under  $10^{-3}/\text{s}$ ,  $10^{-4}/\text{s}$ ,  $10^{-5}/\text{s}$  and  $10^{-6}/\text{s}$  conditions at  $550\ ^\circ\text{C}$ : (a) SLM HB, (b) SLM VB and (c) forged specimens. The loading directions of HB and VB specimens and building direction are also illustrated in (a) and (b).



**Table 2**

Slow strain rate tensile test results at 550 °C.

	Strain rate/s	Yield strength (0.2% proof)/MPa	Ultimate strength/MPa	Fracture strain/%	Environmental fracture area/%
SLM HB	$10^{-3}$	1166	1273	14.7	0
	$10^{-4}$	1184	1293	15.1	0
	$10^{-5}$	1157	1293	6.4	0.84
	$10^{-6}$	1151	1227	2.5	4.91
SLM VB	$10^{-4}$	1078	1223	16.1	0
	$10^{-6}$	1095	1203	10.1	2.35
Forged	$10^{-3}$	1109	1270	19.0	0
	$10^{-4}$	1109	1281	19.0	0
	$10^{-5}$	1089	1299	20.3	5.33
	$10^{-6}$	1106	1245	7.9	15.28

**Table 3**

Slow strain rate tensile test results at 650 °C.

	Strain rate/s	Yield strength (0.2% proof)/MPa	Ultimate strength/MPa	Fracture strain/%	Environmental fracture area/%
SLM HB	$10^{-3}$	1085	1172	5.0	- <sup>a</sup>
	$10^{-4}$	1068	1126	2.7	- <sup>a</sup>
	$10^{-5}$	–	980	0.76	- <sup>a</sup>
	$10^{-6}$	–	778	0.47	- <sup>a</sup>
SLM VB	$10^{-4}$	1077	1127	9.7	- <sup>a</sup>
	$10^{-6}$	902	922	4.7	- <sup>a</sup>
Forged	$10^{-3}$	1086	1202	29.0	4.95
	$10^{-4}$	1038	1144	14.7	31.59
	$10^{-5}$	996	1048	11.8	82.48
	$10^{-6}$	928	937	19.3	- <sup>a</sup>

<sup>a</sup> Unable to clearly define the environment-assisted intergranular fracture areas due to the presence of other intergranular damage.

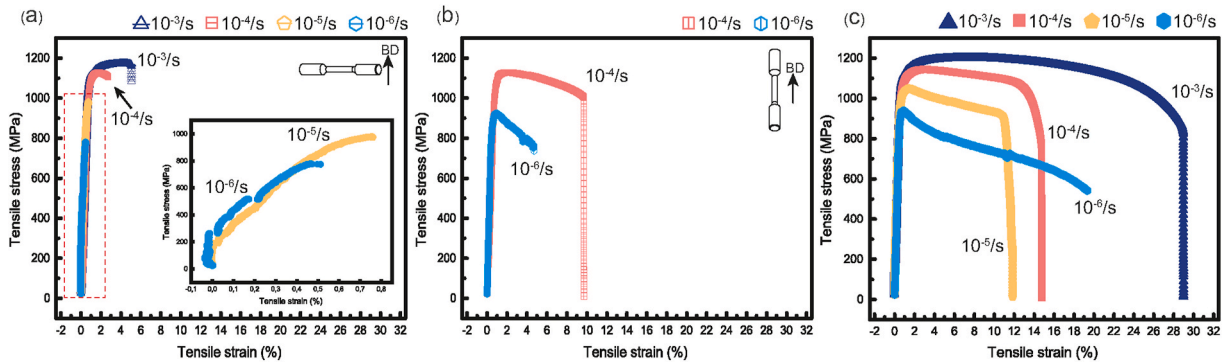


**Fig. 4.** Tensile stress-strain curves under  $10^{-3}/s$ ,  $10^{-4}/s$ ,  $10^{-5}/s$  and  $10^{-6}/s$  conditions at 650 °C: (a) SLM HB, (b) SLM VB and (c) forged specimens. The insert in (a) is the enlarged tensile curves for the  $10^{-5}/s$  and  $10^{-6}/s$  conditions. The loading directions of HB and VB specimens and building direction are also illustrated in (a) and (b).

ductility (see Table 3). Such environmental effects on the strain rate dependent ductility has also been reported in Mattiello et al. (2019). The typical environment-assisted intergranular fracture on forged specimen is shown in Fig. 7c. However, with further reducing the strain rate to  $10^{-6}/s$ , the environment-assisted intergranular degradation seems to be almost inactive, but another damage mode results in completely intergranular fracture as well.

Fractured cross sections, especially the microstructures beneath the fracture surface will be compared between the strain rates of  $10^{-4}/s$  and  $10^{-6}/s$  at 550 and 650 °C, to understand the damage development with decreasing strain rate.

### 3.4. Fracture development at $10^{-4}/s$ strain rate

The cross sections of SLM HB, SLM VB and forged specimens tested at  $10^{-4}/s$  strain rate at 550 °C and 650 °C are shown in Fig. 8 and Fig. 9, respectively. All microstructures at both 550 °C and 650 °C show significant plastic deformation, as evidenced by the back scatter electron contrast in the SEM images. At 550 °C, micro voids can be found along some grain boundaries and associated with grain boundary  $\delta$  phases in the SLM HB specimens (Fig. 8b). For comparison, fewer micro voids can be found in the SLM VB specimen, and forged counterpart seem to be completely free of grain boundary micro voids.

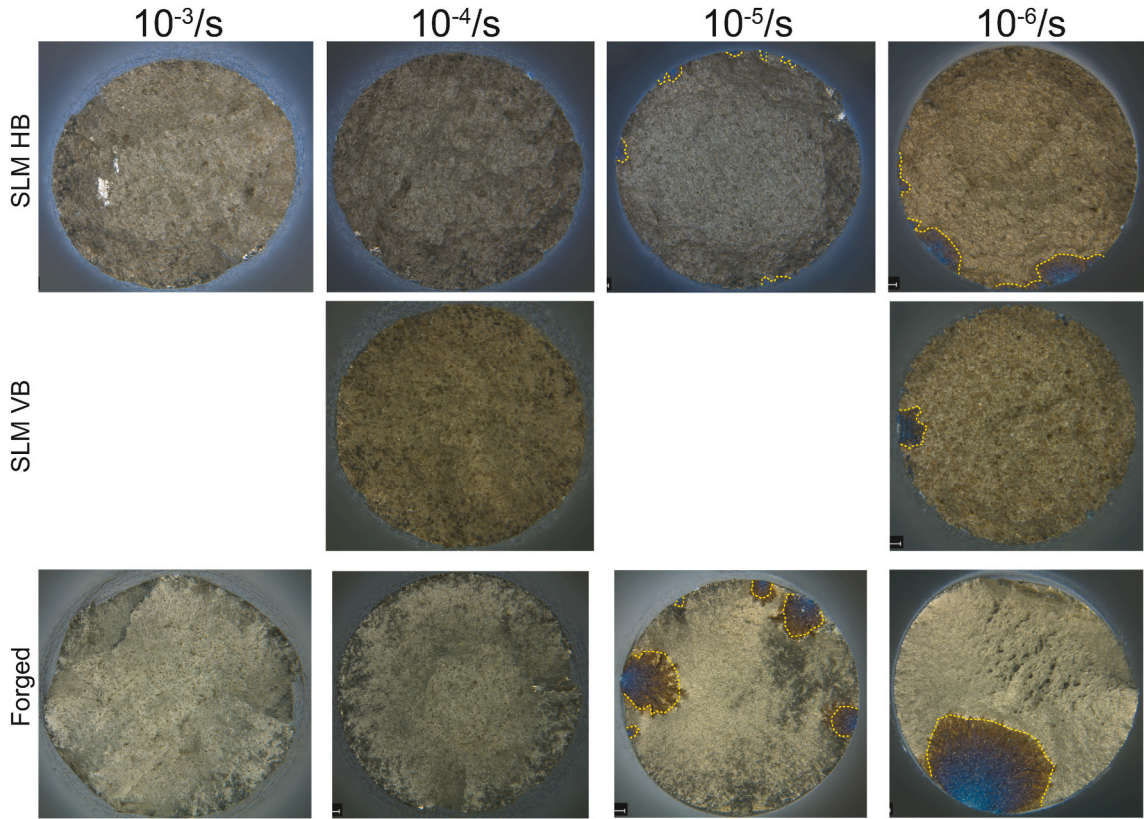


**Fig. 5.** Fracture surfaces of SLM HB, SLM VB and forged specimens fractured at  $10^{-3}/s \sim 10^{-6}/s$  strain rate at  $550^\circ\text{C}$ .

At  $650^\circ\text{C}$ , micro voids at grain boundaries and coalescence of voids and formation of cracks are easily found in the SLM HB and VB specimens (see Fig. 9a and c). Comparison between SLM HB and VB specimens shows that: intergranular cavities and crack mostly concentrate near the fracture surface in SLM HB specimen; while in the SLM VB specimen interconnected cracks are present a few hundred microns away from fracture surface, and cracks are in larger amount and are more open up. For the forged specimen, all the cracks found are connected to the fracture surface, and the cracks propagate in a brittle de-cohesion way by environment-assisted grain boundary embrittlement (see Fig. 9f). Such a cracking behaviour in forged material is noticeably different to that in SLM materials shown in Fig. 9b and d.

### 3.5. Fracture development at $10^{-6}/s$ strain rate

With reducing the strain rate to  $10^{-6}/s$ , intergranular cracks are present in both SLM HB and SLM VB specimens at  $550^\circ\text{C}$ , and it seems that there are more intergranular cracks in the SLM VB specimen than in the SLM HB specimen (comparing Fig. 10a and c). Such intergranular cracks seem to develop by coalescence of micro voids at the grain boundaries, as evidenced in Fig. 10b and d. No micro voids at grain boundaries or intergranular cracks can be found in the forged specimen.

The microstructures of tests at the  $650^\circ\text{C}$  and  $10^{-6}/s$  strain rate are of particular interest, due to the very different tensile responses between the three specimens. The SLM HB specimen, which fractures immediately at the macro yielding point and underwent almost no macro plastic deformation, shows generally little deformation contrast (see Fig. 11a). One can also find the continuous intergranular crack as well as discontinuous micro voids (see Fig. 11b).

The SLM VB specimen generally shows significant plastic deformation, and the intergranular cracks and grain boundary micro voids are in larger amount and more open-up and interconnected than that of HB specimens. This is consistent with the comparison between  $550^\circ\text{C}$  cases.

The forged specimens tested at  $650^\circ\text{C}$  and  $10^{-6}/s$  strain rate shows the most significant plastic deformation contrast among all the specimens (see Fig. 11 f). Grains are largely deformed, and grain boundary can be barely identified by the grain boundary  $\delta$  phases. Extremely small ( $\sim 100$  nm) cavities are present at these less-well defined grain boundaries, possibly causing the intergranular fracture as consistent with the fractography inspection. This cavitation process is attributed to the plastic (creep) flow under elevated temperature, rather than the environment-assisted grain boundary embrittlement.

Combining the stress-strain curves, fractography and cross section inspections, the most noticeable differences in the strain-rate dependent deformation behaviours between SLM and forged materials are:



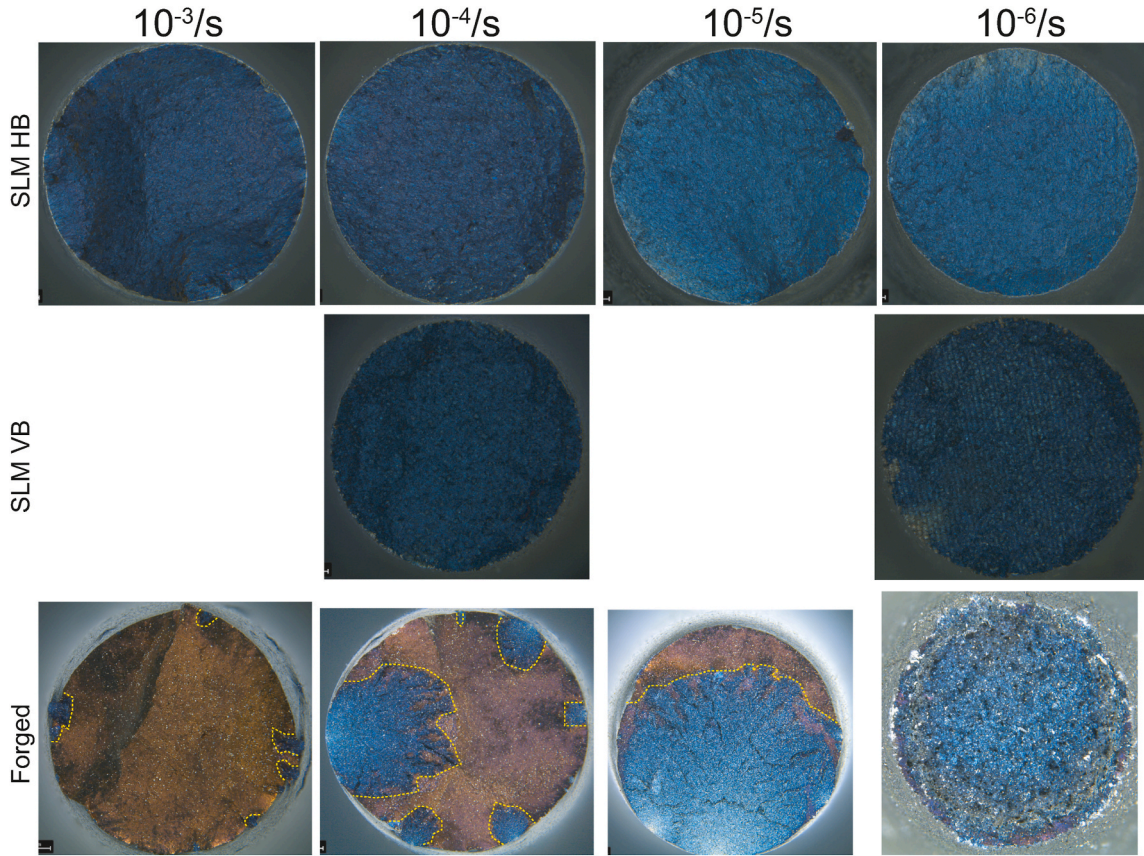


**Fig. 6.** Fracture surfaces of SLM HB, SLM VB and forged specimens fractured at  $10^{-3}/s \sim 10^{-6}/s$  strain rate at 650 °C.

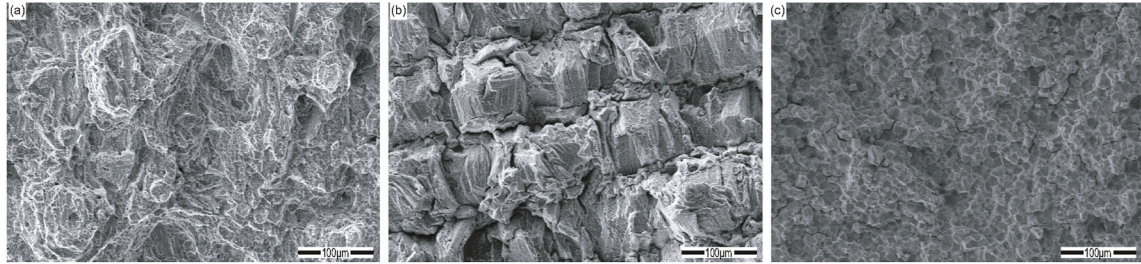


**Fig. 7.** (a) Dimpled intergranular fracture on the SLM HB specimen tested at  $10^{-6}/s$  and 650 °C; (b) Smooth intergranular fracture on the SLM VB specimen tested at  $10^{-6}/s$  and 650 °C; (c) Environment-assisted intergranular fracture on the forged specimen tested at  $10^{-5}/s$  and 650 °C.

1. SLM material shows significant ductility degradation due to an intergranular cavitation process as strain rate is decreased, while the environment-assisted grain boundary embrittlement does not progress proportionally to the ductility degradation.
2. Forged material firstly shows ductility degradation proportional to the environment-assisted grain boundary embrittlement when decreasing strain rates. Further decreasing strain rate will render ductility recovery due to the overwhelming plastic (creep) flow.

The deformation behaviours observed in the forged materials are in accordance and explained in the literatures (Sugahara et al., 2012; Khan and Yu, 2012). In the following discussion, the aim is to address the ductility degradation mechanism of the SLM material which is not clear yet, using the forged counterpart as a control.



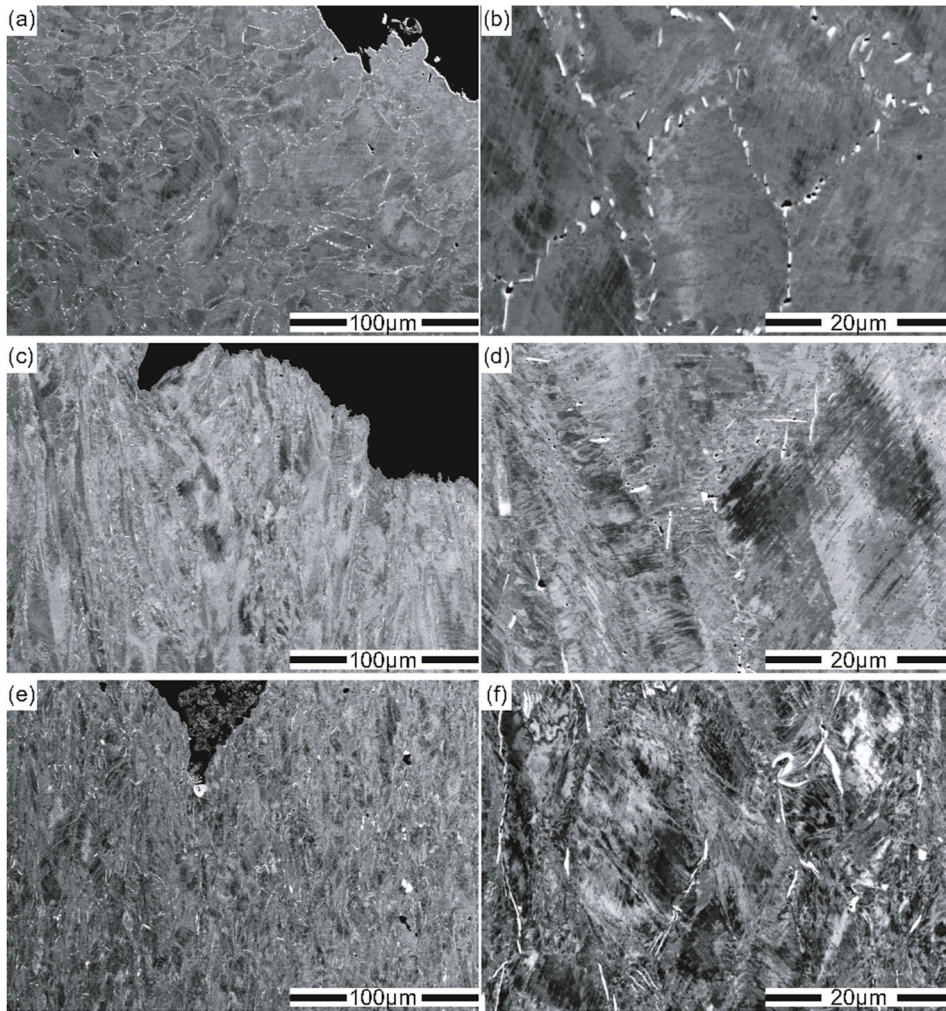


**Fig. 8.** Fracture cross sections of (a) SLM HB, (c) SLM VB and (e) forged specimens tested at  $10^{-4}$ /s strain rate at 550 °C. (b), (d) and (f) are the enlarged reviews from (a), (c) and (e), respectively.

## 4. Discussion

### 4.1. Ductility degradation in the SLM materials

#### 4.1.1. Rule out of the environmental effect

The progressive environmental effect is less likely the main reason for ductility reduction in the SLM materials. As commonly observed, intergranular cavities or cracks are discontinuous and far beneath from the fracture surfaces (see Fig. 10a and b, Fig. 11a and b) in the SLM materials. If cracking those grain boundaries was by environmental degradation, the long-range diffusion of oxygen from the open fracture surface to the cracked grain boundaries should be required, probably via grain boundary diffusion. Such a diffusion process would have surely damaged or embrittled those grain boundaries (between the fracture surface and the underlying cracked grain boundaries) on the diffusion path, while they are still intact as observed. One might also question about the possibility of oxygen pick up during the SLM process, which leads to the 'dynamic embrittlement' and ductility reduction in SLM materials. It was found that processing under argon with 800 ppm or 20 ppm oxygen did not significantly affect the oxygen pick up in SLM 316L (Pauzon et al., 2019). More importantly, if oxygen pick up was assumed during processing, it would have been expected that the SLM IN718 grain boundaries have been already 'dynamic embrittled' before the tensile tests. Under that assumption, the ductility is supposed to be less independent of strain rate, namely, fracture happens as long as the stress is high enough to break the 'embrittled' grain boundaries; and at the strain rate of  $10^{-3}$ /s the ductility is supposed to be lowest since stress increases most rapidly to the maximum. This strongly indicates other damage mechanisms excluding the environmental degradation mechanism. Another evidence can be provided in the cracking behaviour in Fig. 9: the typical environment-assisted cracking is essentially a brittle de-cohesion process (Fig. 9f), while the SLM grain boundaries are cracked by growth and coalescence of micro voids (Fig. 9b and d), which is not brittle but plastic.



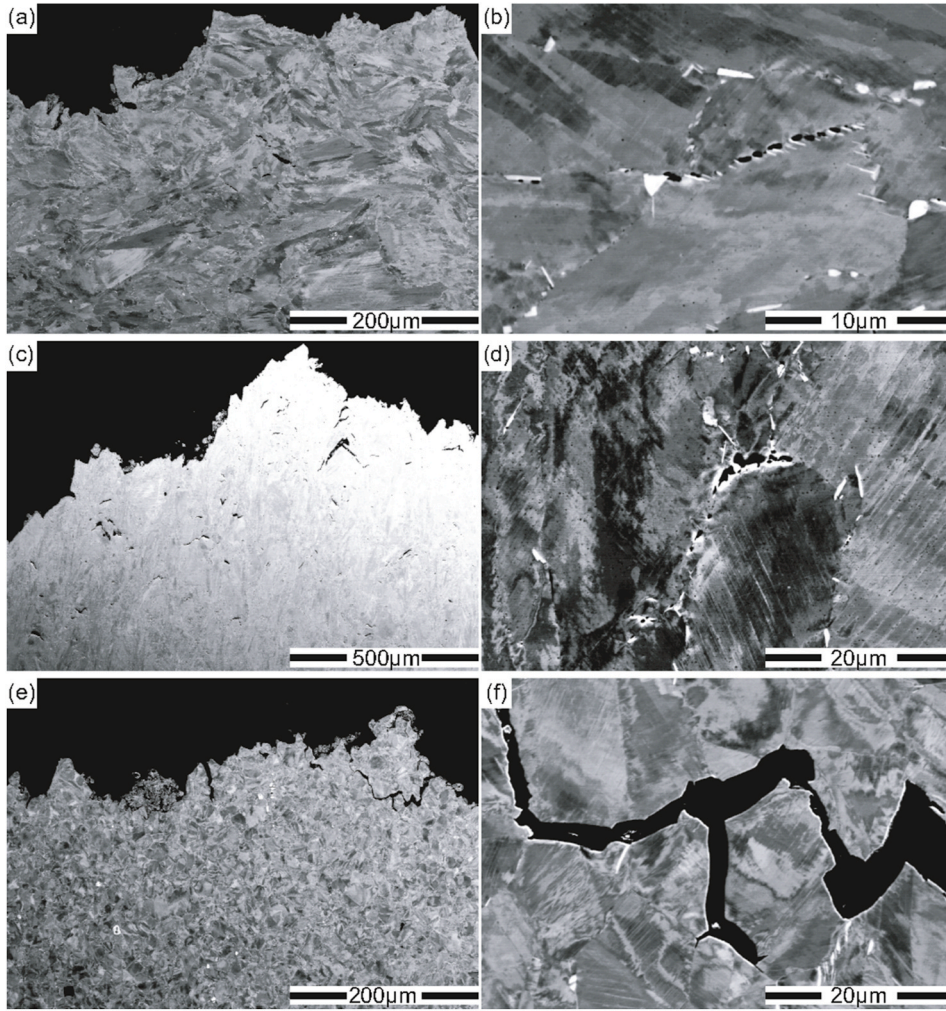


**Fig. 9.** Fracture cross sections of (a) SLM HB, (c) SLM VB and (e) forged specimens tested at  $10^{-4}$ /s strain rate at 650 °C. (b), (d) and (f) are the enlarged reviews from (a), (c) and (e), respectively.

#### 4.1.2. Rule out of the $\delta$ phase effect

On the other hand, the SLM intergranular cracks or precursor micro grain boundary voids are usually associated with  $\delta$  precipitates, as shown in Figs. 8b and 9b. One might have to consider the possibility of de-bonding of such  $\delta$  precipitates at grain boundaries. Additional SSRT experiments have been done on a HA (1080 °C homogenization + standard double ageing) heat-treated SLM HB specimens at 550 °C. The HA heat treatment gives ignorable amount of  $\delta$  precipitates at the grain boundaries. Generally, HA specimens show identical tensile properties and fracture features to HSA specimens. Interestingly, as shown in Fig. 12, discontinuous micro voids also form and coalesce at the  $\delta$ -free grain boundaries in HA specimen, similar to the cases with HSA cases with  $\delta$  at grain boundaries. This suggests that  $\delta$  precipitates are not the principal cause for forming cavities at grain boundaries.

Therefore, the ductility degradation in the SLM materials is mainly caused by a time-dependent intergranular cavitation process. In addition, the comparison on ductilities under different strain rates and temperatures between SLM HB and VB specimens also indicates that stress can assist the cavitation process. The cavitation process is more accelerated at grain boundaries aligning perpendicular to the loading direction than at grain boundaries aligning parallel to loading direction. These features strongly indicate that such a time-dependent cavitation process is creep damage.

#### 4.2. Creep damage

Now that creep is assumed to be the main damage mechanism for the SLM materials during slow strain rate tests, it is of great interest to compare the creep rate between SLM and conventional counterparts under creep loading conditions. Creep tests are usually performed under constant stress  $\sigma_{creep, const}$  and the creep rate  $\dot{\epsilon}_{creep}$  of interest is the dependent variable. While in the slow strain rate tests in the present study, strain rate  $\dot{\epsilon}_{SSRT, const}$  is constant and stress  $\sigma_{SSRT}$  is the dependent variable. A proper approximation is needed

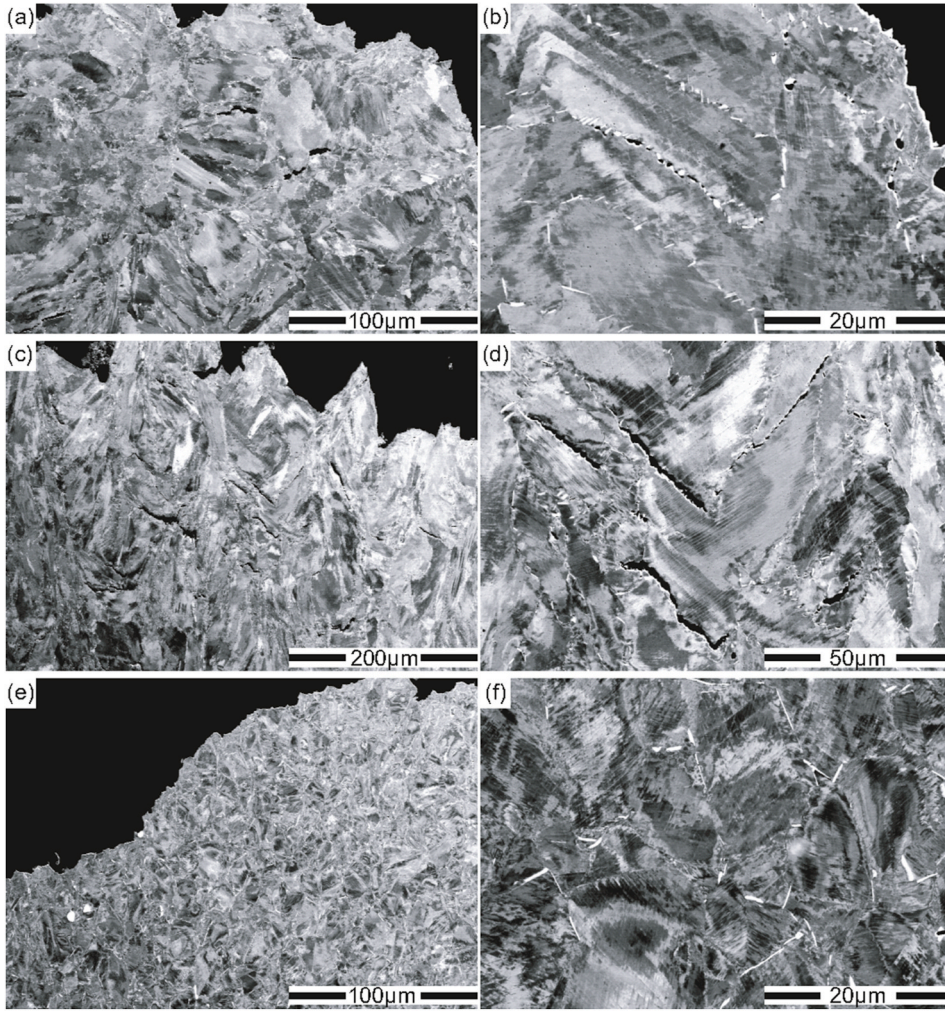


**Fig. 10.** Fracture cross sections of (a) SLM HB, (c) SLM VB and (e) forged specimens tested at  $10^{-6}$ /s strain rate at 550 °C. (b), (d) and (f) are the enlarged reviews from (a), (c) and (e), respectively.

to infer the creep properties from the slow strain rate tests.

From the creep practice experience, the minimum creep rate of interest can usually be obtained at the creep strain of 1%. On the stress-strain curves in Figs. 3 and 4, the 1% plastic strain is approximately at about 2% total strain, if the fracture strain is above 2%. On the other hand, creep test is usually performed under stress lower than the monotonic tensile strength, giving relatively low creep strain rate. Given that, the following approximation considers only the cases of  $10^{-6}$ /s strain rate at 550 °C, and  $10^{-5}$ /s  $\sim 10^{-6}$ /s strain rate at 650 °C in the present study. In the following discussion, the flow stress  $\sigma_{\text{SSRT}, 2\%}$  is taken at 2% total strain and combined with corresponding strain rate  $\dot{\epsilon}_{\text{SSRT}, \text{const}}$  to approximate the minimum creep rate  $\dot{\epsilon}_{\text{creep}, \text{minimum}}$  under the constant stress  $\sigma_{\text{creep}, \text{const}}$ .

$$\begin{aligned}\sigma_{\text{SSRT}, 2\%} &\simeq \sigma_{\text{creep}, \text{const}} \\ \dot{\epsilon}_{\text{SSRT}, \text{const}} &\simeq \dot{\epsilon}_{\text{creep}, \text{minimum}}\end{aligned}$$

For the SLM HB  $10^{-5}$ /s and  $10^{-6}$ /s at 650 °C cases, which break before total strains reach 2%, the maximum stresses before failure are considered. The approximated creep data is summarized in Table 4.

#### 4.2.1. Comparison with creep data

One surprising observation from the present study is that the SLM materials undergo creep damage even at the temperature of 550 °C, which is usually too low to consider the activation of creep damage for Ni-base superalloys (Drexler et al., 2018). For comparison, creep process is not active in the forged counterparts at any strain rates tested at 550 °C. Due to the limit creep data available for IN718 at the temperature of 550 °C, the present study uses the Minimum Commitment Method (MCM) model and the equation constants determined by Brinkman et al. (1991), to get the creep data. The MCM model is in the form of:



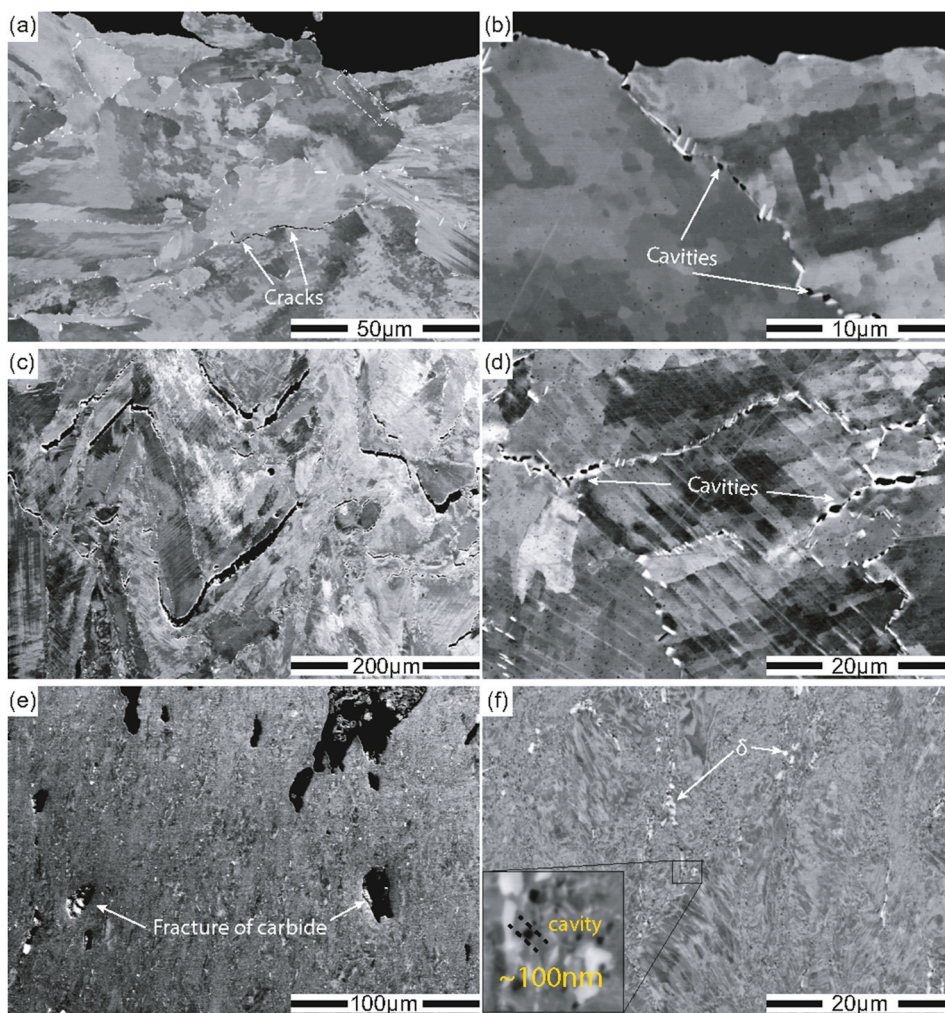


**Fig. 11.** Fracture cross sections of (a) SLM HB, (c) SLM VB and (e) forged specimens tested at  $10^{-6}$ /s strain rate at 650 °C. (b), (d) and (f) are the enlarged reviews from (a), (c) and (e), respectively.

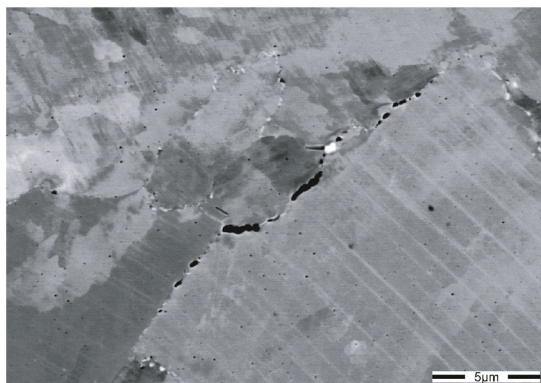


**Fig. 12.** Grain boundary voids at  $\delta$ -free grain boundary in HA specimen tested at  $10^{-6}$ /s and 550 °C.

**Table 4**

Approximate creep data inferred from slow strain rate tests.

Sample	Approx. Creep rate/s	Flow stress/MPa at 2% strain	
		550 °C	650 °C
SLM HB	10 <sup>-5</sup>	–	979 <sup>a</sup>
	10 <sup>-6</sup>	1227	778 <sup>a</sup>
SLM VB	10 <sup>-6</sup>	1193	877
Forged	10 <sup>-5</sup>	–	1040
	10 <sup>-6</sup>	1228	889

<sup>a</sup> Maximum stress before failure is adapted since total strains is less than 2%.

$$\lg t_r + \left[ R_1(T - T_{middle}) + R_2 \left( \frac{1}{T} - \frac{1}{T_{middle}} \right) \right] = A_h + B_h \lg \sigma + D\sigma + E\sigma^2 \quad (1)$$

where  $t_r$  is rupture life in hour,  $\sigma$  is stress in MPa,  $T$  is temperature in K and  $T_{middle}$  equals to 867 K. The constants  $R_1$ ,  $R_2$ ,  $D$  and  $E$  were determined to be  $2.14547 \times 10^{-2}$ ,  $-5622.73$ ,  $-2.71294 \times 10^{-3}$  and  $-2.96015 \times 10^{-6}$  respectively.  $A_h$  and  $B_h$  are two lot constants that neglecting the heat treatment variations, and are 9.66956 and  $-0.899187$  respectively after average. These aforementioned constants were statistically determined from 264 experimental test results and showed overall good description of stress rupture behaviour for IN718 (Brinkman et al., 1991).

With the rupture time  $t_r$  determined from the MCM model, the average creep rate  $\dot{\epsilon}_{ss}$  to the onset of tertiary creep can be deduced from the following relationship (Brinkman et al., 1991):

$$\dot{\epsilon}_{ss} = B t_r^{-\alpha} \quad (2)$$

where  $B$  and  $\alpha$  were constants and given as 2.142 and 1.151 respectively. By Equations (1) and (2), trend lines of average creep rate versus stress at 550 and 650 °C are calculated by setting stresses within reasonable ranges that yield the average creep rate ranges of  $10^{-11} \sim 10^{-6}$ /s and  $10^{-11} \sim 10^{-5}$ /s, respectively. Fig. 13 presents the calculated trend lines, comparing with the approximate experimental data points of forged and SLM samples deduced from the present tests.

As compared in Fig. 13, one can note that the average creep rate of SLM material is comparable to the conventional counterpart at 550 °C but is generally inferior at 650 °C. It is also noted that the creep ductility seems to play a more significant role than the creep rate in the creep behaviour for the SLM materials, since the extremely poor ductility limits the flow stress that the test can achieve, especially at 650 °C SLM HB cases. In Fig. 13 the minimum creep rates of SLM IN718 from McLouth et al. (2020); Otsuka et al. (2018) are also included. Similar to the SSRT results, even though the minimum creep rates are comparable, the creep ductilities in McLouth et al. (2020); Otsuka et al. (2018) are much inferior to the wrought counterparts tested at the same conditions. If better ductility can be achieved, the flow stress of the SLM HB specimen at the same average creep rate is supposed to be comparable to that of the conventional counterparts. In Wang et al. (2019) the comparable creep properties have been reported for SLM and conventional IN718 at the creep rate  $\sim 8 \times 10^{-5}$ /s at 650 °C, at which strain rate condition ductility is not significantly degraded as shown in Fig. 4. Even for the SLM VB specimen, the continuous decrease of flow stress at  $10^{-6}$ /s and 650 °C is mainly due to the intergranular cavitation and loss of load-bearing area, rather than extensive creep/plastic flow (e.g. recover and recrystallization). Otherwise, one would have expected the better ductility in that case. Therefore, to understand the nominal ‘inferior creep resistance’ of SLM materials, it is essentially to understand *what is the cause for rapid cavitation at SLM grain boundaries?*

#### 4.2.2. Cavitation at SLM grain boundaries

**4.2.2.1. Nucleation and growth/coalescence.** Cavitation of a grain boundary during creep test includes both nucleation and growth/coalescence processes. For the SLM HB specimen at 550 °C, intergranular cavities (see Fig. 8) can be easily found even at the relatively high strain rate of  $10^{-4}$ /s, at which condition the time to fracture upon loading is short. Therefore, the nucleation seems to be rather rapid for the SLM materials at elevated temperatures. Once a cavity nuclei is formed, under the simultaneous effects of stress and thermal activation, the cavity nuclei starts to grow and coalesce.

The growth of intergranular cavities can be controlled by diffusion flow, creep (plastic deformation) flow and a coupling of diffusion and creep flows (Cocks and Ashby, 1982). The essence of cavity growth at grain boundary by diffusion flow is that certain matter diffuses out from the growing void or vacancy diffuses into the cavity, which is driven by the chemical potential gradient of the diffusing matter around the growing void at the stressed state (Cocks and Ashby, 1982). Cavity growth by plastic flow is due to that the material around the cavity nuclei is plastically stretched, increasing the cavity’s volume (Cocks and Ashby, 1982; Nix et al., 1983).

Note that, at 650 °C, intergranular fracture by cavitation happens without macro plastic flow for the SLM HB cases at the strain rate of  $10^{-6} \sim 10^{-5}$ /s (see Fig. 4a). This strongly indicates that, at 650 °C stress-assisted diffusion flow alone is able to result in significant cavity growth and coalescence and therefore a fully intergranular fracture. Differently, since plasticity is present for all SLM specimens within the tested strain rates at 550 °C, it is not possible to clarify if at this temperature, stress-assisted diffusion flow alone can result in the similar fully intergranular fracture as at 650 °C. Probably, plastic flow does not play a decisive role in the cavitation process, even though it can accelerate the cavitation process. Instead, time, especially effective diffusion time, is the critical factor for the cavitation



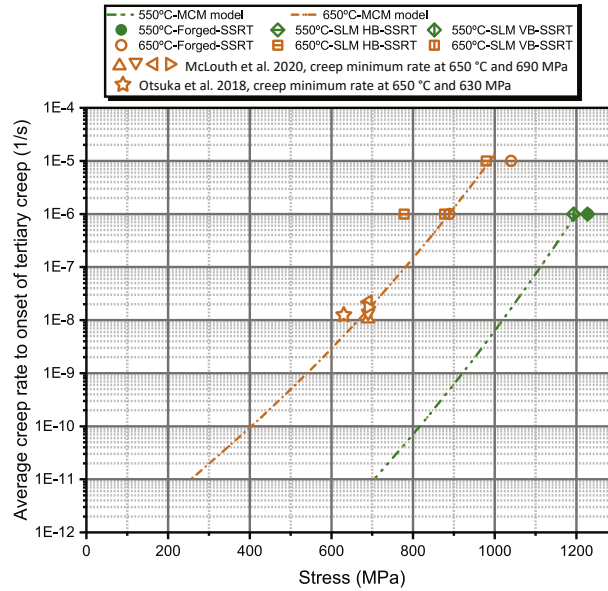


**Fig. 13.** Plot of stress versus average creep rate. The dash and dot lines are calculated with the MCM model at 550 and 650 °C. The forged and SLM SSRT data are approximated and presented for comparison of creep resistance. Creep minimum rate data from McLouth et al. (McLouth et al., 2020) and Otsuka et al. (Otsuka et al., 2018) are also included for comparison.

and fracture strain. That means, if the sample is hold under stress (constant or not, above yield or not) at elevated temperature for enough time, the stress-assisted diffusion process will result in noticeable cavitated grain boundaries and premature fracture.

**4.2.2.2. Nucleation: critical factor for the inferiority.** Aforementioned, once the cavity is nucleated, the stress-assisted diffusion alone can cause the growth and coalescence of cavities and further the fracture. Therefore, assuming the time to fracture is constant and loading is the same, the shorter nucleation time, the longer growth and coalescence time and the better-developed/interconnected intergranular cracks. Obviously, the cavity nucleation rate is relatively rapid at the SLM grain boundaries, which is the critical factor for the susceptibility of creep damage of the SLM materials. It is evident from the comparison between the cross sections in Fig. 11 that: the intergranular cavity at the forged grain boundary is still extremely small even though it underwent such large plastic deformation and long time to fracture.

**Table 5**

Parameters and values used in evaluating nucleation rate.

Parameter	Value	Comment and Reference
$\Gamma$	2J/m <sup>2</sup>	Ref. (Seitzman et al., 1986)
$\Omega$	10 <sup>-29</sup> m <sup>3</sup>	Ref. (Frost and Ashby, 1982)
$\Sigma$	1.2 × 10 <sup>9</sup> Pa	arbitrary, above yielding in SSRT
$D_B\delta$	1.58 × 10 <sup>-22</sup> m <sup>3</sup> /s	$D_B\delta = D_{0B}\delta \times \exp\left(-\frac{Q_B}{RT}\right)$ where $D_{0B}\delta = 3.15 \times 10^{-15}$ m <sup>3</sup> /s $Q_B = 115$ kJ/mol, Ref. (Frost and Ashby, 1982)
$T$	823K	
$K$	1.38 × 10 <sup>-23</sup> m <sup>2</sup> Kg · s <sup>-2</sup> K <sup>-1</sup>	
$\rho_{max}$	2.87 × 10 <sup>16</sup> m <sup>-2</sup>	$\rho_{max} = 1/\left[\bar{r}_c^2 F_B(\alpha)\right]$ $\bar{r}_c \approx r_c, \text{ where } r_c \text{ is the critical radius}$ $\text{given by } r_c = \frac{2\gamma}{\sigma}, \text{ Ref. (Raj and Ashby, 1975)}$
$F_v$	4.18	$F_v(\alpha) = \frac{2\pi}{3} (2 - 3\cos\alpha + \cos^2\alpha), \alpha = 90^\circ, \text{ Ref. (Raj and Ashby, 1975)}$
$F_B$	3.14	$F_B(\alpha) = \pi \sin^2\alpha, \alpha = 90^\circ, \text{ Ref. (Raj and Ashby, 1975)}$

4.2.2.3. *Why rapid cavity nucleation for SLM materials?* Raj et al. (Raj and Ashby, 1975) proposed a theoretical model to address the nucleation rate  $\dot{\rho}$  as:

$$\dot{\rho} = \frac{4\pi\gamma}{\Omega^{4/3}\sigma} D_B \delta \left(1 + \frac{\delta\Omega}{kT}\right) (\rho_{max} - \rho) \cdot \exp \left[ - \left( \frac{4\gamma^3 F_V(\alpha)}{\sigma^2 kT} \right) \right] \quad (3)$$

where  $\gamma$  is the free surface energy (per unit area) of the cavity,  $\Omega$  is the atomic volume,  $D_B \delta$  is the boundary diffusion coefficient times the boundary thickness,  $k$  is the Boltzmann constant,  $T$  is the temperature in K,  $\frac{\delta\Omega}{kT}$  is usually  $\ll 1$ ,  $\rho_{max}$  is the maximum number of potential nucleation sites in the grain boundary per unit area, and  $\rho$  is the number of nucleation sites,  $F_V(\alpha) = \frac{2\pi}{3} (2 - 3\cos\alpha + \cos^3\alpha)$  is a geometry function and  $\alpha$  is the contact angle between the void surface and the grain boundary. Due to the difficulties in clearly separating cavity nucleation from cavity growth and coalescence, the nucleation time or nucleation rate can not be clarified from the present SSRT data. However, given that the forged grain boundaries have considerable low cavity nucleation rate compared to the SLM grain boundaries, we can still qualitatively discuss the possible factors that has the most significant importance for the nucleation rate.  $\gamma$ ,  $\Omega$  and  $D_B \delta$  are adapted from literatures for nickel.  $F_V$  and  $F_B$  are calculated at  $\alpha = 90^\circ$ , assuming the nucleation is at a grain boundary with the stress perpendicular to it and the shape of the void is spheric. This excludes the scenarios of nucleation at stress concentration at three-grain-junctions and at inclusions. This assumption also reflects the nucleation for the SLM HB specimen, see for example Fig. 9b.  $\sigma$  is set arbitrarily above yield strength for the enhancement of nucleation. For the maximum nucleation rate, the number of nucleation sites  $\rho$  is set to zero. Numerically, the exponential has the most significant effect on the magnitude of nucleation rate. With parameters listed in Table 5, the calculated exponential is essentially zero and so is the nucleation rate at 1200 MPa and 550 °C. That indicates cavity nucleation at grain boundary should not occur at the condition, which is consistent with the present experimental observation for the forged counterparts.

By decreasing the surface energy  $\gamma$  to a reasonable level, it is possible to increase the exponential from nearly-zero to non-zero as shown in Table 6, and thereby to a noticeable nucleation rate. Assuming that cavity growth is ignorable at the strain rate of  $10^{-4}$ /s and at 550 °C for the SLM HB sample due to the limited time (1694s upon loading to fracture), the quantity of cavities measured from the fractured cross-section per unit area by image analysis and divided by the loading time is a rough estimation of nucleation rate  $\dot{\rho}$ , which is at the order of  $10^6 \text{m}^{-2}\text{s}^{-1}$ . Such a nucleation rate requires a surface energy of about 0.2 J/m<sup>2</sup>. As shown in Table 6, it is noticed that even a slight decrease in surface energy  $\gamma$  can lead to a dramatic increase of nucleation rate  $\dot{\rho}$  in a few order of magnitudes.

Noticeable reduction of surface energy can be achieved by segregation or adsorption of certain impurities in trace amount at grain boundaries, which decreases the nucleation barrier and assists void nucleation to occurs rapidly (Shewmon and Anderson, 1998). Therefore, the local segregation of trace elements at grain boundaries can be a possible cause for the rapid cavitation nucleation in the present SLM cases. Beneficial effects of phosphorus (P) and boron (B) and detrimental effects of sulphur (S) on creep properties of forged IN718 have been reported in Xie et al. (1996); Hu et al. (2000); Li et al. (2006). Generally, S remarkably reduces the creep ductility at 650 °C. However, it should be noticed that even though with a 175 ppm addition of S in the forged IN718 in Xie et al. (1996), 5% of stress rupture elongation can still be achieved at 650 °C and 686 MPa. For comparison, the lowest ductility is only 0.47% for SLM HB specimen at 650 °C in the present study. Given that the master powders' chemical composition for the SLM builds is carefully controlled as per AMS 5662 and below the aforementioned 175 ppm S, such an inferior ductility of SLM materials can not be simply attributed to the segregation of trace elements at grain boundary. Instead, other microstructure features might contribute simultaneously to the ductility inferiority. As showed in Fig. 2b, the as-heat-treated SLM material typically has the cell/subgrain feature, which actually presents a highly deformed state introduced by the complicated thermal history during manufacturing process (Deng et al., 2019; Witzen et al., 2020; Bronkhorst et al., 2019), resulting in a non-equilibrium or energetically metastable state of the grain boundary (Tucker and McDowell, 2011). Possibly, the fact that how this deformed microstructure interacts with segregation of trace elements dynamically under loading is a more important key to understand the inferior ductility inferiority. Characterization of the segregation behaviours of trace elements at grain boundaries, especially at the atomic scale level, is out of the scope of the present study but is of interest for the future work.

## 5. Conclusions

Slow strain rate tests have been performed on SLM HB, VB and forged IN718 at strain rates of  $10^{-3}$ /s  $\sim$   $10^{-6}$ /s and at temperatures

**Table 6**  
The dependence of exponential and nucleation rate on surface energy.

Surface Energy $\gamma$ (J/m <sup>2</sup> )	$\exp \left[ - \left( \frac{4\gamma^3 F_V(\alpha)}{\sigma^2 kT} \right) \right]$	$\rho_{max}$ (m <sup>-2</sup> )	Nucleation rate $\dot{\rho}$ (m <sup>-2</sup> s <sup>-1</sup> )	Note
2	0	2.87E+16	0	$\frac{4\pi\gamma}{\Omega^{4/3}\sigma} \sim \text{E}+30$ $D_B \delta \sim \text{E}-22$ $1 + \frac{\delta\Omega}{kT} \approx 1$
1.5	0	5.10E+16	0	
1	0	1.15E+17	0	
0.5	3.17E-56	4.59E+17	1.45E-46	
0.4	3.84E-29	7.17E+17	2.75E-19	
0.3	1.03E-12	1.27E+18	1.31E-2	
0.2	2.81E-4	2.87E+18	8.04E+6	
0.1	0.36	1.15E+19	4.12E+10	

of 550 °C and 650 °C. Systematic fractography and microstructure studies have been done to correlate the time-dependent damage mechanism in the SLM and forged IN718. The main conclusions can be summarized as following:

1. Within the test strain rates and temperatures, SLM materials are rather susceptible to creep damage and intergranular fracture by cavity nucleation and growth. With decreasing strain rate and increasing test temperature, ductility degradation is significantly enhanced. For comparison, the forged material mostly shows a progressive environment-assisted grain boundary embrittlement with decreasing strain rate. Creep damage in the forged counterparts is active only at  $10^{-6}$ /s strain rate and at 650 °C.
2. The creep resistance, especially regarding the average creep rate and creep stress, is approximated from the SSRT data: at 550 °C both SLM HB and VB specimen have the same average creep rate to the conventional counterpart at the same stress level; at the 650 °C, the SLM VB specimen is barely comparable to the conventional counterpart, while the SLM HB is much inferior.
3. Cavity nucleates rapidly at SLM grain boundaries under loading in SLM materials. Growth and coalescence of cavities lead to inferior ductility and premature intergranular fracture of SLM materials when decreasing strain rate at elevated temperature.
4. Intragranular plastic deformation does not seem necessary to nucleate cavity at SLM grain boundaries at elevated temperature. Low surface energy is probably the most critical factor for the rapid cavity nucleation and the inferior ductility for SLM materials

#### Autho statement

**Dunyong Deng:** Investigation, Formal analysis, Writing- Original draft preparation. **Ru Lin Peng:** Formal analysis, Writing- Reviewing and Editing, Supervision. **Johan Moverare:** Conceptualization, Methodology, Formal analysis, Writing- Reviewing and Editing, Supervision, Funding acquisition.

#### Declaration of competing interest

The authors declare that they have no known competing financial interests or personal relationships that could have appeared to influence the work reported in this paper.

#### Acknowledgements

Siemens Energy AB is acknowledged for providing test materials in the present study. Faculty grant SFO-MAT-LiU#2009-00971 from Linköping University and Swedish Governmental Agency for Innovation Systems (Vinnova grant 2016-05175) are also acknowledged for financial support.

#### References

- Balachandramurthi, A.R., Moverare, J., Dixit, N., Pederson, R., 2018. Influence of defects and as-built surface roughness on fatigue properties of additively manufactured alloy 718. *Mater. Sci. Eng. A* 735, 463–474.
- Balachandramurthi, A.R., Moverare, J., Dixit, N., Deng, D., Pederson, R., 2019. Microstructural influence on fatigue crack propagation during high cycle fatigue testing of additively manufactured alloy 718. *Mater. Char.* 149, 82–94.
- Basirat, M., Shrestha, T., Potirniche, G., Charit, I., Rink, K., 2012. A study of the creep behavior of modified 9cr–1mo steel using continuum-damage modeling. *Int. J. Plast.* 37, 95–107.
- Brinkman, C., Booker, M., Ding, J., 1991. Creep and creep-rupture behavior of alloy 718. In: *Superalloys 718,625 and Various Derivatives 1991*, the Minerals. Metals & Materials Society, pp. 519–536.
- Bronkhorst, C.A., Mayeur, J.R., Livescu, V., Pokharel, R., Brown, D.W., Gray III, G.T., 2019. Structural representation of additively manufactured 316l austenitic stainless steel. *Int. J. Plast.* 118, 70–86.
- Chlebus, E., Gruber, K., Kuźnicka, B., Kurzac, J., Kurzynowski, T., 2015. Effect of heat treatment on the microstructure and mechanical properties of inconel 718 processed by selective laser melting. *Mater. Sci. Eng. A* 639, 647–655.
- Choi, I.-C., Kim, Y.-J., Seok, M.-Y., Yoo, B.-G., Kim, J.-Y., Wang, Y., Jang, J.-i., 2013. Nanoscale room temperature creep of nanocrystalline nickel pillars at low stresses. *Int. J. Plast.* 41, 53–64.
- Cocks, A., Ashby, M., 1982. On creep fracture by void growth. *Prog. Mater. Sci.* 27 (3–4), 189–244.
- Deng, D., Peng, R.L., Brodin, H., Moverare, J., 2018. Microstructure and mechanical properties of inconel 718 produced by selective laser melting: sample orientation dependence and effects of post heat treatments. *Mater. Sci. Eng. A* 713, 294–306.
- Deng, D., Eriksson, R., Peng, R.L., Moverare, J., 2019. On the dwell-fatigue crack propagation behavior of a high-strength ni-base superalloy manufactured by selective laser melting. *Metall. Mater. Trans.* 1. <https://doi.org/10.1007/s11661-019-05548-8>.
- Deng, D., Peng, R.L., Moverare, J., 2020. A comparison study of the dwell-fatigue behaviours of additive and conventional IN718: The role of dislocation substructure on the cracking behaviour. *Mater. Sci. Eng. A* 797, 140072.
- Drexler, A., Fischerswöring-Bunk, A., Oberwinkler, B., Ecker, W., Ganser, H.-P., 2018. A microstructural based creep model applied to alloy 718. *Int. J. Plast.* 105, 62–73.
- Frost, H.J., Ashby, M.F., 1982. *Deformation Mechanism Maps: the Plasticity and Creep of Metals and Ceramics*. Pergamon press.
- Ghorbanpour, S., Alam, M.E., Ferreri, N.C., Kumar, A., McWilliams, B.A., Vogel, S.C., Bicknell, J., Beyerlein, I.J., Knezevic, M., 2020. Experimental characterization and crystal plasticity modeling of anisotropy, tension-compression asymmetry, and texture evolution of additively manufactured inconel 718 at room and elevated temperatures. *Int. J. Plast.* 125, 63–79.
- Henthorne, M., 2016. The slow strain rate stress corrosion cracking test—a 50 year retrospective. *Corrosion* 72 (12), 1488–1518.
- Hu, Z., Song, H., Guo, S., Sun, W., 2000. Role of p, s and b on creep behavior of alloy in 718. *Cailiao Kexue Yu Jishu*(J. Mater. Sci. Technol.)(China)(USA) 17, 399–402.
- Jia, Q., Gu, D., 2014. Selective laser melting additive manufacturing of inconel 718 superalloy parts: densification, microstructure and properties. *J. Alloys Compd.* 585, 713–721.
- Khan, A.S., Yu, S., 2012. Deformation induced anisotropic responses of ti–6al–4v alloy. part i: Experiments. *Int. J. Plast.* 38, 1–13.
- Krupp, U., 2008. Improving the resistance to intergranular cracking and corrosion at elevated temperatures by grain-boundary-engineering-type processing. *J. Mater. Sci.* 43 (11), 3908–3916.

- Krupp, U., Kane, W.M., Liu, X., Dueber, O., Laird, C., McMahon Jr., C.J., 2003. The effect of grain-boundary-engineering-type processing on oxygen-induced cracking of In718. *Mater. Sci. Eng. A* 349 (1–2), 213–217.
- Krupp, U., Kane, W., Laird, C., McMahon, C., 2004. Brittle intergranular fracture of a ni-base superalloy at high temperatures by dynamic embrittlement. *Mater. Sci. Eng. A* 387, 409–413.
- Krupp, U., Wagenhuber, P.-G., Kane, W., McMahon, C., 2005. Improving resistance to dynamic embrittlement and intergranular oxidation of nickel based superalloys by grain boundary engineering type processing. *Mater. Sci. Technol.* 21 (11), 1247–1254.
- Krupp, U., Wackermann, K., Christ, H.-J., Colliander, M.H., Stiller, K., 2017. Intergranular oxidation effects during dwell-time fatigue of high-strength superalloys. *Oxid. Metals* 88 (1), 3–14.
- Kuo, Y.-L., Horikawa, S., Kakehi, K., 2017. Effects of build direction and heat treatment on creep properties of ni-base superalloy built up by additive manufacturing. *Scripta Mater.* 129, 74–78.
- Kuo, Y.-L., Kamigaichi, A., Kakehi, K., 2018a. Characterization of ni-based superalloy built by selective laser melting and electron beam melting. *Metall. Mater. Trans.* 49 (9), 3831–3837.
- Kuo, Y.-L., Nagahari, T., Kakehi, K., 2018b. The effect of post-processes on the microstructure and creep properties of alloy718 built up by selective laser melting. *Materials* 11 (6), 996.
- Li, N., Sun, W., Xu, Y., Guo, S., Lu, D., Hu, Z., 2006. Effect of p and b on the creep behavior of alloy 718. *Mater. Lett.* 60 (17–18), 2232–2235.
- Li, Z., Voisin, T., McKeown, J.T., Ye, J., Braun, T., Kamath, C., King, W.E., Wang, Y.M., 2019. Tensile properties, strain rate sensitivity, and activation volume of additively manufactured 316L stainless steels. *Int. J. Plast.* 120, 395–410.
- Li, Z., Li, Z., Tan, Z., Xiong, D.-B., Guo, Q., 2020. Stress relaxation and the cellular structure-dependence of plastic deformation in additively manufactured AlSi10Mg alloys. *Int. J. Plast.* 127, 102640.
- Lindström, T., Ewest, D., Simonsson, K., Eriksson, R., Lundgren, J.-E., Leidermark, D., 2020. Constitutive model of an additively manufactured ductile nickel-based superalloy undergoing cyclic plasticity. *Int. J. Plast.* 102752.
- Lu, Y., Wu, S., Gan, Y., Huang, T., Yang, C., Junjie, L., Lin, J., 2015. Study on the microstructure, mechanical property and residual stress of slm Inconel-718 alloy manufactured by differing island scanning strategy. *Optic Laser. Technol.* 75, 197–206.
- Mattielo, A., Desmorat, R., Cormier, J., 2019. Rate dependent ductility and damage threshold: application to nickel-based single crystal CMSX-4. *Int. J. Plast.* 113, 74–98.
- McLouth, T.D., Witkin, D.B., Bean, G.E., Sitzman, S.D., Adams, P.M., Lohser, J.R., Yang, J.-M., Zaldivar, R.J., 2020. Variations in ambient and elevated temperature mechanical behavior of In718 manufactured by selective laser melting via process parameter control. *Mater. Sci. Eng. A* 780, 139184.
- Morra, P., Radelaar, S., Yandouzi, M., Chen, J., Böttger, A., 2009. Precipitate coarsening-induced plasticity: low temperature creep behaviour of tempered SAE 52100. *Int. J. Plast.* 25 (12), 2331–2348.
- Nix, W., Yu, K., Wang, J., 1983. The effects of segregation on the kinetics of intergranular cavity growth under creep conditions. *Metall. Trans. A* 14 (3), 563–570.
- Otsuka, T., Wakabayashi, H., Igarashi, D., Ariaseta, A., Imano, S., Wang, Y., Kobayashi, S., Takeyama, M., 2018. Effect of homogenization on creep of additively manufactured alloy 718. *Proceedings of the 9th International Symposium on Superalloy 718 & Derivatives: Energy, Aerospace, and Industrial Applications*. Springer International Publishing, Cham, pp. 501–513.
- Pauzon, C., Hryha, E., Forêt, P., Nyborg, L., 2019. Effect of argon and nitrogen atmospheres on the properties of stainless steel 316 L parts produced by laser-powder bed fusion. *Mater. Des.* 179, 107873.
- Pei, C., Shi, D., Yuan, H., Li, H., 2019. Assessment of mechanical properties and fatigue performance of a selective laser melted nickel-base superalloy Inconel 718. *Mater. Sci. Eng. A* 759, 278–287.
- Popovich, V., Borisov, E., Heurtebise, V., Riemsdijk, T., Popovich, A., Sufiarov, V.S., 2018. Creep and thermomechanical fatigue of functionally graded Inconel 718 produced by additive manufacturing. In: *TMS Annual Meeting & Exhibition*. Springer, pp. 85–97.
- Raj, R., Ashby, M., 1975. Intergranular fracture at elevated temperature. *Acta Metall.* 23 (6), 653–666.
- Schlesinger, M., Seifert, T., Preussner, J., 2017. Experimental investigation of the time and temperature dependent growth of fatigue cracks in Inconel 718 and mechanism based lifetime prediction. *Int. J. Fatig.* 99, 242–249.
- Seitzman, L., Wang, L., Kulcinski, G., Dodd, R., 1986. The effect of oxygen on void stability in nickel and austenitic steel. *J. Nucl. Mater.* 141, 738–742.
- Shewmon, P., Anderson, P., 1998. Void nucleation and cracking at grain boundaries. *Acta Mater.* 46 (14), 4861–4872.
- Shi, J., Li, X., Zhang, Z., Cao, G., Russell, A., Zhou, Z., Li, C., Chen, G., 2019. Study on the microstructure and creep behavior of Inconel 718 superalloy fabricated by selective laser melting. *Mater. Sci. Eng. A* 765, 138282.
- Sugahara, T., Martinoli, K., Reis, D.A., de Moura Neto, C., Couto, A.A., Neto, F.P., Barboza, M., 2012. Creep behavior of the Inconel 718 superalloy. In: *Defect and Diffusion Forum*, vol. 326. Trans Tech Publ, pp. 509–514.
- Trosch, T., Ströbner, J., Völkl, R., Glatzel, U., 2016. Microstructure and mechanical properties of selective laser melted Inconel 718 compared to forging and casting. *Mater. Lett.* 164, 428–431.
- Tucker, G.J., McDowell, D.L., 2011. Non-equilibrium grain boundary structure and inelastic deformation using atomistic simulations. *Int. J. Plast.* 27 (6), 841–857.
- Wang, H., Dhiman, A., Ostergaard, H.E., Zhang, Y., Siegmund, T., Kruzic, J.J., Tomar, V., 2019. Nanoindentation based properties of Inconel 718 at elevated temperatures: a comparison of conventional versus additively manufactured samples. *Int. J. Plast.* 120, 380–394.
- Witkin, D., Patel, D., Bean, G., 2019a. Notched fatigue testing of Inconel 718 prepared by selective laser melting. *Fatig. Fract. Eng. Mater. Struct.* 42 (1), 166–177.
- Witkin, D.B., Hayes, R.W., McLouth, T.D., Bean, G.E., 2019b. Anomalous notch rupture behavior of nickel-based superalloy Inconel 718 due to fabrication by additive manufacturing. *Metall. Mater. Trans.* 50 (8), 3458–3465.
- Witzen, W.A., Polonsky, A.T., Pollock, T.M., Beyerlein, I.J., 2020. Three-dimensional maps of geometrically necessary dislocation densities in additively manufactured ni-based superalloy In718. *Int. J. Plast.* 102709.
- X. Xie, X. Liu, Y. Hu, B. Tang, Z. Xu, J. Dong, K. Ni, Y. Zhu, S. Tien, L. Zhang, et al., The Role of Phosphorus and Sulfur in Inconel 718, *Superalloys 1996* 599.
- Xu, Z., Hyde, C., Tuck, C., Clare, A., 2018. Creep behaviour of Inconel 718 processed by laser powder bed fusion. *J. Mater. Process. Technol.* 256, 13–24.
- Xu, J., Gruber, H., Deng, D., Peng, R.L., Moverare, J.J., 2019. Short-term creep behavior of an additive manufactured non-weldable nickel-base superalloy evaluated by slow strain rate testing. *Acta Mater.* 179, 142–157.
- Yoo, B.-G., Kim, J.-Y., Kim, Y.-J., Choi, I.-C., Shim, S., Tsui, T.Y., Bei, H., Ramamurty, U., Jang, J.-i., 2012. Increased time-dependent room temperature plasticity in metallic glass nanopillars and its size-dependency. *Int. J. Plast.* 37, 108–118.
- Zhang, D., Niu, W., Cao, X., Liu, Z., 2015. Effect of standard heat treatment on the microstructure and mechanical properties of selective laser melting manufactured Inconel 718 superalloy. *Mater. Sci. Eng. A* 644, 32–40.